www.adeepakpublishing.com

Holmlund, C. et al. (2020): JoSS, Vol. 9, No. 2, pp. 911–920
(Peer-reviewed article available at www.jossonline.com)

www. JoSSonline.com

Control Electronics for High Wavelength Accuracy in a Nanosatellite Hyperspectral Imager

Christer Holmlund, Antti Näsilä, and Jussi Mäkynen

VTT Technical Research Centre of Finland Ltd
Espoo, Finland

Abstract

Nanosatellite-compatible miniaturized hyperspectral imagers must achieve excellent wavelength accuracy in order to provide data suitable for use in scientific missions. This paper presents the gap control of the Fabry-Perot interferometer (FPI) used in the hyperspectral imager of the nanosatellite Aalto-1. The imager uses the FPI as a variable band-pass filter by varying the gap between the mirrors. The distance between the mirrors is estimated by measuring the capacitance between three sets of electrodes positioned around the mirrors. Without temperature compensation, the gap controller was not able to keep the temperature drift of the gap within the specified limit of 0.3 nm/°C. The gap control loop was broken down into potential drift contributors, and the worst-case instability is estimated. The measured drift was larger than the estimated drift, probably due to deformation of the FPI substrates. Using a temperature compensation function in the instrument microcontroller software, the resulting drift was reduced by more than an order of magnitude, satisfying the requirement.

1. Introduction

Small satellites are generating a rapid change in the application of space technologies. Cost-efficient small satellites can form constellations, and together they can acquire data more flexibly than traditional satellites. This means significant new opportunities for Earth observation.

However, current sensing technologies developed for traditional large satellites are not suitable for use in small satellites, due to the size and mass of these instruments. Miniaturization of key sensing technologies presents a challenge for the development of suitable payloads.

VTT Technical Research Centre of Finland has developed piezo-actuated Fabry-Perot interferometer (FPI) tunable optical filters for various wavelength ranges from the ultraviolet to the thermal infrared. When combined with imaging sensors, this technology is able to create small, light-weight hyperspectral cameras. Unlike traditional satellites' push broom instruments, which require stable attitude control, these 2D snapshot hyperspectral imagers are able to operate on platforms with relaxed stability requirements, such as nanosatellites and UAVs.

The tunable Fabry-Perot interferometer used in these imagers essentially consists of two plane

Corresponding Author: Christer Holmlund – Christer.holmlund@vtt.fi

mirrors, facing each other with a small, parallel, adjustable gap between them. The FPI is placed in the optical path of the imager and transmits light only at narrow wavelength bands (Mannila et al., 2013).

Many applications of tunable Fabry-Perot interferometers in, for example, astronomy and atmospheric and so-lar physics, require a large optical aperture. Rees et al. (1981) report on control of capacitance-stabilized FPIs with working diameters of 150 mm. Compared to these, the FPI used in the Aalto-1 Spectral Imager, and discussed in this paper, is a dwarf; the longest side of the entire imager measures 97 mm (Näsilä, 2013).

Reaktor Space Lab's nanosatellite Hello World, launched in December 2018, carries the first ever near-infrared hyper-spectral imager on a nanosatellite (Reaktor Space Labs, 2019). This imager uses an FPI with many resemblances to the one used on Aalto-1.

Several satellite instruments using light-weight, low-order, capacitance-stabilized FPIs were under construction during the spring of 2019, including, for example, the atmospheric limb-sounding instrument ALTIUS (Remy et al., 2019) and the ozone monitoring instrument VISION on the nanosatellite PICASSO (Saari et al., 2015; Näsilä, 2016), while others were on the drawing board, such as the Asteroid Spectral Imaging Mission ASPECT (Kohouta et al., 2018).

Wavelength accuracy and stability are two of the most important properties of the hyperspectral imager. This work reports on the electronics design concept for ensuring accurate control of the FPI mirror gap in the Aalto-1 spectral imager.

2. Concept of the Aalto-1 Hyperspectral Imager

The Aalto-1 Spectral Imager is one of three payload instruments of Aalto University's nanosatellite Aalto-1, launched in June 2017. The imager, made by VTT Technical Research Centre of Finland, is a full-frame, staring, hyperspectral camera recording images at one, two, or three wavelength bands per exposure. In addition to the hyperspectral camera, the imager contains also a normal RGB camera with higher spatial resolution. The Aalto-1 satellite is based on the CubeSat concept and occupies three units. The size of the spectral imager is half a cube unit, 97 x 97 x 48 mm^3, and its mass is 600 g (Näsilä, 2013).

The Fabry-Perot interferometer (FPI), used as wavelength selection filter, essentially consists of two plane mirrors facing each other with a small, parallel gap between them (Mannila et al., 2013). In a tunable FPI, the distance between the mirrors, the gap, is adjustable. With three piezo-electric actuators placed between the mirror substrates, the distance and parallelism can be controlled. The position of the mirrors is estimated by measuring the capacitance between electrodes deposited on the substrates around the mirror areas, close to the actuators. The capacitance signals are used as inputs to a closed-loop control system driving the voltages of the piezo actuators.

The tunable Fabry-Perot interferometer (FPI) is used for wavelength selection in the spectral imager. The FPI is placed in the optical path of the imager, and transmits light only at narrow wavelength bands.

The image of the object is projected onto an RGB CMOS image sensor, a CMOSIS CMV4000. This sensor has an active area of 2048 x 2048 pixels, but the imager uses only a center portion of 1024 x 1024 pixels. The image is further digitally binned to a final size of 512 x 512 pixels (Kestilä et al., 2013). Due to the known spectral sensitivities of the red, green, and blue pixels, up to three wavelengths can be recorded in each exposure. Only one wave-length is freely selectable; the other ones represent neighboring orders of interference of the FPI for the selected gap.

To record a spectral data cube, the FPI is adjusted to a gap giving transmission bands at the desired wavelengths. The global shutter image sensor is triggered and read out. The next gap in the sequence is set, the sensor is again triggered, and so on until images at all wavelengths in the cube have been recorded.

In the Earth-observing satellite Aalto-1, normally a sequence of 14 gaps is used. The exposure time is typically 5 ms, and a complete data cube is acquired in 500 ms. As all the images of the data cube are not exposed simultaneously, the images need registration in the post-processing phase.

The total wavelength range of the spectral imager is limited by long- and short-pass filters to 500 … 900 nm, i.e., from blue-green to the near infrared.

3. The Fabry-Perot Interferometer (FPI)

In the Aalto-1 instrument, the FPI is operated at low order, below seven, with gap widths between 350 and 2000 nm. The FPI is used as an adjustable optical comb filter with one, two, or three transmission bands within the operating wavelength range of 500 ... 900 nm.

The gap of the FPI is adjusted using three piezoelectric actuators mounted directly between the mirror substrates. The gap between the mirror surfaces can be adjusted in the range 0.35 … 2.0 µm by changing the actuator drive voltages between 20 and 110 V. Closed-loop control of the gap is necessary to achieve the required stability and mirror parallelism. The FPI mirror gap is estimated by measuring the capacitance between three sets of electrodes deposited outside the optically active mirror areas (Figure 1).

The following sections present the capacitive gap measurement and the control system of the FPI, an assessment of temperature-induced effects on the gap control, and finally, temperature-induced stability measurements performed on the Aalto-1 Spectral Imager.

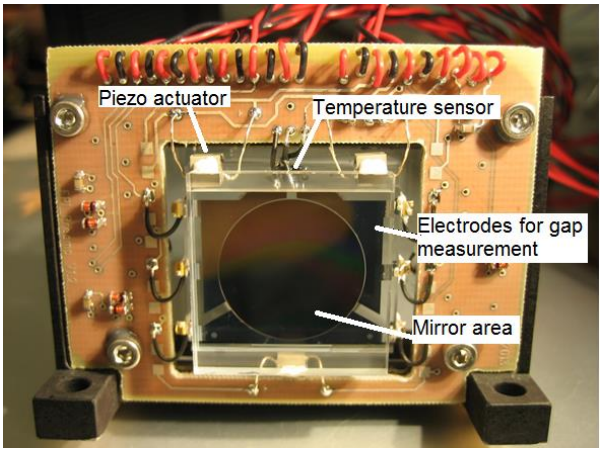

Figure 1. The FPI mounted with its preamplifier board in the support frame.

4. Gap Measurement

The FPI gap is controlled by balancing a capacitive half-bridge (Figure 2). The capacitance C_{fpi} represents the capacitance between the electrodes deposited on the FPI substrates; C_{ref} is a discrete capacitor on the preamplifier board; and C_{par} represents parasitic capacitances and the error amplifier input capacitance. V_{ref} is a reference voltage with fixed amplitude, V_{sp} is a variable setpoint voltage, and V_{err} the resulting error or imbalance signal. The aim of the control loop is to adjust the distance between the substrates of the FPI, and thereby C_{fpi}, so that with a given excitation voltage the bridge is balanced, and the voltage V_{err} equals zero.

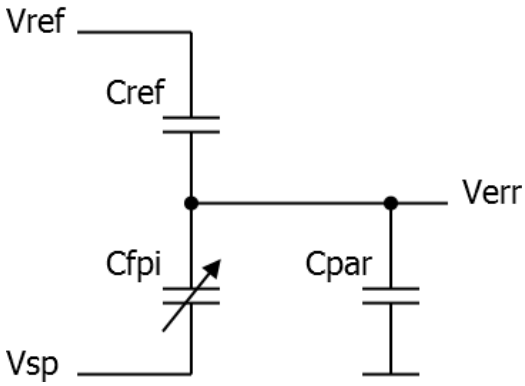

Figure 2. Principle of the FPI capacitive measurement bridge.

Using Laplace transform designators, the error voltage can be expressed as

$$V_{err}(s) = \frac{V_{sp}(s)\, sC_{fpi} + V_{ref}(s)\, sC_{ref}}{sC_{fpi} + sC_{ref} + sC_{par}}. \qquad (1)$$

If the gap controller, acting on C_{fpi}, can balance the bridge and $s(C_{fpi} + C_{ref} + C_{par}) \neq 0$, Eqn. (1) reduces to

$$V_{sp}(s)\, C_{fpi} + V_{ref}(s)\, C_{ref} = 0. \qquad (2)$$

If the ratio of capacitances does not equal the ratio V_{fpi}/V_{ref}, the bridge is not balanced and an error signal is produced. A further condition for balance is that the excitation waveforms are equal, only having different amplitudes,

$$V_{sp}(s) = -k\, V_{ref}(s), \quad k \geq 0. \qquad (3)$$

Often, sine voltages are used for bridge excitation (Hicks et al., 1984). In this case, however, the waveforms are square. The reason is the simple circuitry

needed to produce the excitation waveforms; a square wave with fixed amplitude for the reference signal, and three adjustable square waves for the setpoints, all generated by analog switches (Figure 3).

The voltage feeding the fixed reference capacitor, C_{ref}, in the upper arm is generated by switching between a constant reference voltage and ground. The measurement capacitance, C_{fpi}, is also fed from a switch, here connected between ground and the buffered output of a digital-to-analog converter (DAC). The switches are driven by a common clock at opposite phases. The DAC output is proportional to the reference voltage and the digital setpoint value generated by the instrument microcontroller. This configuration aims at a ratiometric measurement in which the absolute value of the reference voltage is not critical. The gap setpoint or command value is fed as input to the DAC.

5. The FPI Gap Control Loop

The gap distance and the parallelism of the FPI are controlled by three identical closed loop controllers. The control loop (Figure 3) comprises the measurement electrodes on the FPI substrates, the capacitive measurement bridge, the error amplifiers, the demodulator, the I-controller, the piezo amplifiers, and the piezo actuators determining the distance between the measurement electrodes, thus closing the loop. In control engineering terms the FPI electrodes make up the sensor, while the FPI constitutes the controlled plant.

At balance, when the bridge balance condition in Eqn. (2) is satisfied, the input to the error amplifier is zero and possible variations in the DC reference voltage do not affect the steady state conditions. This also holds for the gain of the error amplifier. On the other hand, the open loop gain, and thus the dynamics of the control loop, are affected. The effect is minor and of only secondary importance. This concept, based on single-input, single-out analog feedback loops, has been used in earlier FPI controllers (Hicks et al., 1984). The main difference between the Aalto-1 implementation and earlier ones is the waveform of the excitation voltages of the capacitance bridge; typically, sine wave excitation has been used. In the Aalto-1 spectral imager, however, the bridge is excited with square wave voltages. Stable square wave voltages can be generated using fewer components and simpler circuitry.

The bridge imbalance signal, a square wave signal at the modulation frequency of 312 kHz, is amplified by the error amplifier and converted to a DC signal by synchronous demodulation in the phase-sensitive detector (PSD). This signal, when low-pass filtered, is proportional to the bridge imbalance. It is fed to the integral controller, amplified by the high-voltage amplifier, and fed to the piezo-electric actuator adjusting the distance between the mirror substrates.

In this control loop, the capacitance bridge creates the summing point at which the feedback signal is subtracted from the command. The actual gap is only represented by the FPI capacitance; there is no baseband

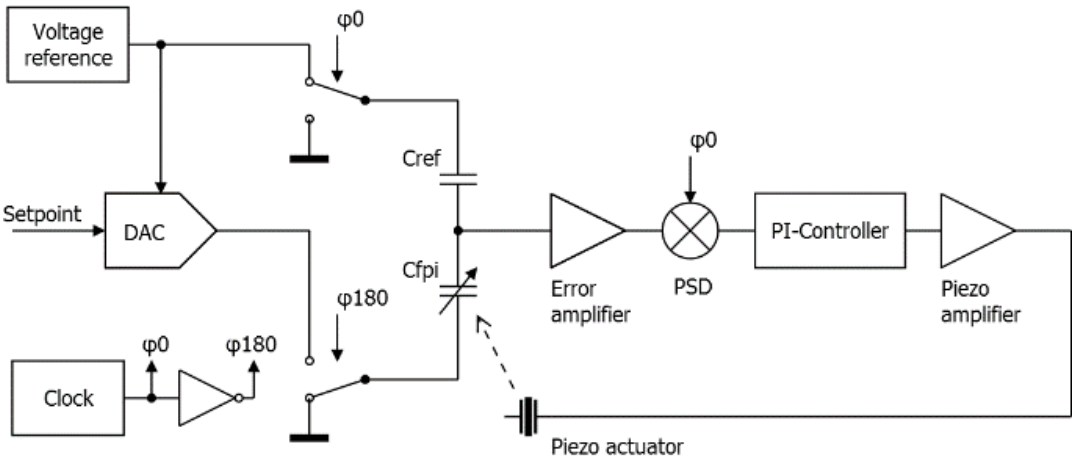

Figure 3. Block diagram of one of the three gap control loops.

signal that is proportional to the gap, only the bridge imbalance signal, the error signal, is available. The setpoints selected for the gap controller always aim to maintain a parallel gap between the optical surfaces. The relation between the three setpoints is determined during calibration by measuring the transmission spectra at different points over the optical aperture, and minimizing the differences.

A block diagram of one of the three identical control loops is shown in Figure 4. The blocks are marked with their transfer function notations. Typical values or transfer functions for each block are given in Table 1. The transfer functions are given as functions of the Laplace variable s. The product of the individual transfer functions gives the loop transfer function, the loop gain. The block transfer functions are not constant, however; the gain of the capacitance bridge depends on the gap, and the transfer function of the piezo actuator and FPI blocks depends on the gas pressure between the FPI mirror substrates. At ambient pressure, the resonance modes of the FPI differ from those in vacuum. For example, the frequency of the dominating resonance in vacuum at 14 kHz increases to 19 kHz at ambient pressure, 100 kPa. The Q-value of this mode is approximately 50 in vacuum, and 30 at ambient pressure. The gap control loop has to be stable during tests in normal pressure as well as in its normal operation environment, vacuum, without parameter changes. The loop gain was therefore set low, just high enough to make the FPI settle between exposures of the image sensor. The loop gain and phase are shown in Figure 5 for two scenarios: a simulated response in

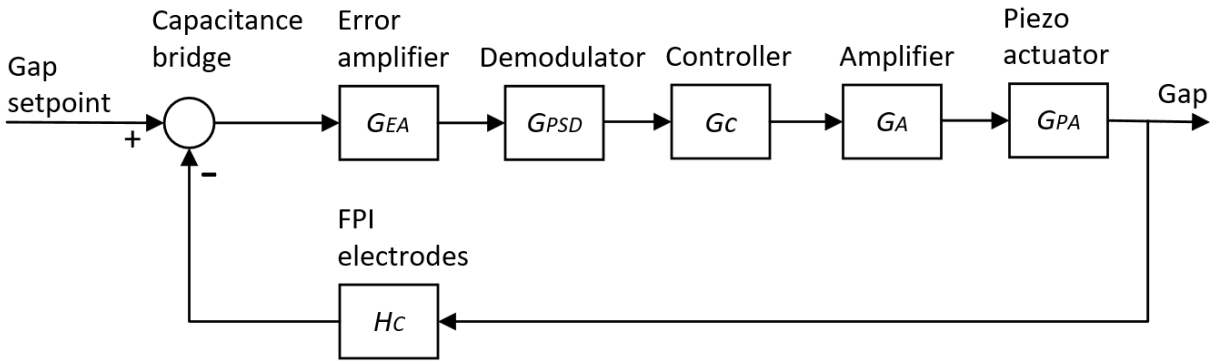

Figure 4. Block Diagram of the Gap Control Loop.

Table 1. Description and Typical Values of the Transfer Function Blocks

Block	Description	Transfer Function	Units used for Transfer Function
G_{BE}	Capacitance bridge and error amplifiers: Capacitance to error voltage	$0.045 \cdot 6.4$	V/pF
G_{PSD}	Demodulator: Amplitude modulated error signal to baseband error voltage	$\frac{0.37}{1.6\text{E-}5\ s + 1}$	V/V
G_C	I-controller: Error voltage to actuation voltage	$\frac{1000}{s}$	V/V
G_A	Piezo amplifier: Actuation to piezo voltage	$\frac{28}{3.1\text{E-}8\ s^2 + 5.7\text{E-}4\ s + 1}$	V/V
G_{PA}	Piezo actuator: Voltage to gap change	$\frac{6.2\text{E}7}{s^2 + 156\ s + 7.7\text{E}9}$	µm/V
H_C	FPI electrodes: Gap change to capacitance change	7.6	pF/µm

vacuum, and a measured response at ambient pressure, both at a mirror gap of 1.5 µm.

The loop gain measurement was made by inserting a test signal in the control loop using an external injection amplifier. The injection amplifier does not change the gain of the loop, but allows injection of a test signal without loading the adjacent blocks. For this measurement, the injection amplifier was inserted between the I-controller and the piezo amplifier. An HP 89410A vector signal analyzer generated the swept sine test signal, and recorded the signals at the output of the I-controller and the input to the piezo amplifier. The ratio of the complex spectra of the recorded signals is presented as the loop gain and phase in Figure 5.

The stability of the closed-loop transfer function from any point in the loop to any other point is characterized by the open-loop transfer function $G(s)\,H(s)$, the product of all the block transfer functions of Figure 4. As long as the value of $G(s)\,H(s) \neq -1$, the closed loop is stable. The main disturbances to the steady state of this control loop are changes in gap setpoint, piezo actuator creep, and thermomechanical effects. For all disturbances, the control loop tries to adjust the gap according to the commanded setpoint.

The stability of the control loop can be assessed using the Bode plot, Figure 5. The magnitude of the complex loop transfer function is expressed in decibels, and the phase angle in degrees. The gain

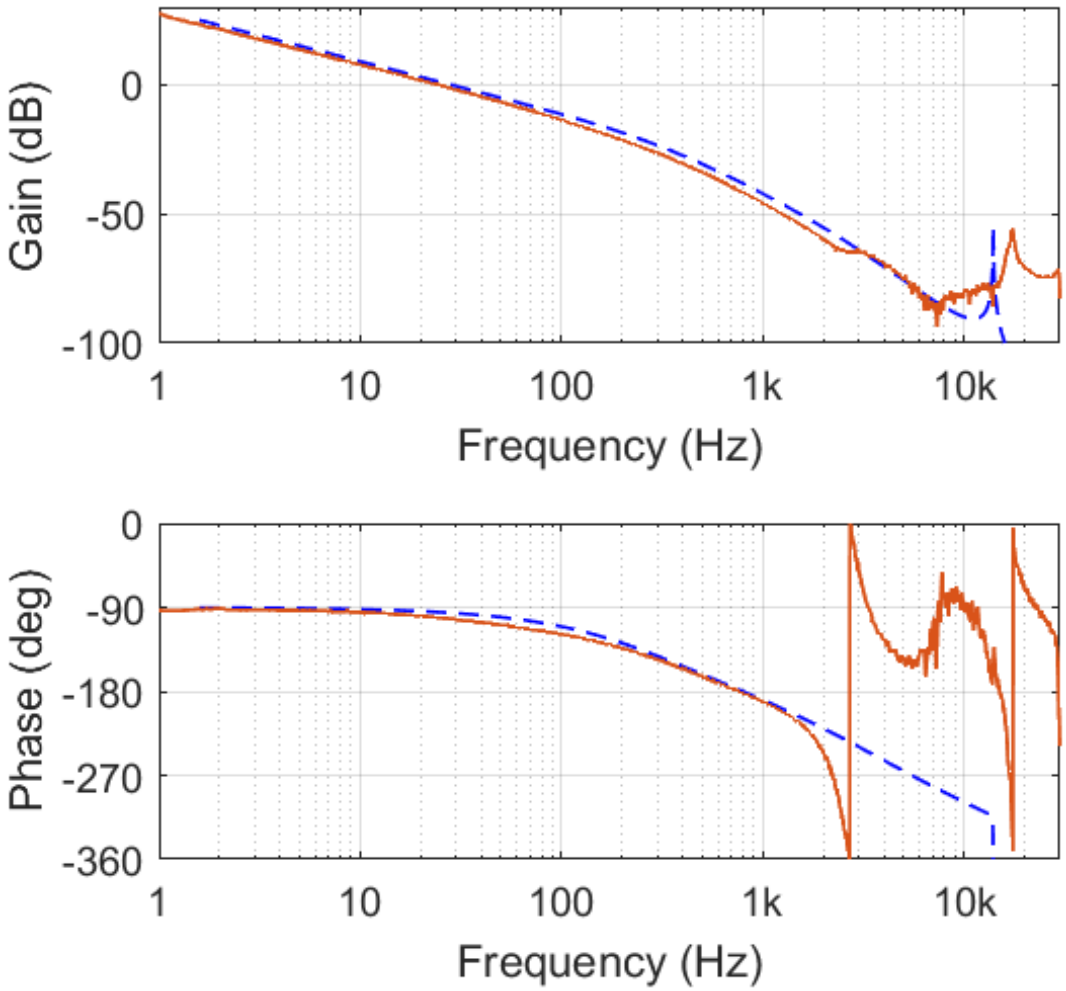

Figure 5. Bode plots of the loop transfer function. Dashed line: simulated in vacuum, solid line: measured at ambient air pressure.

margin, i.e. the additional gain needed to make the loop gain unity, 0 dB, at the frequency giving a phase angle of −180°, is approx. 30 dB. The phase margin, i.e., the phase difference between the phase at the frequency giving a gain of 0 dB, and −180°, is above 75° at the gain crossover frequency of 27 Hz. These values allow ample uncertainties in the block transfer functions without jeopardizing stability of the control loop.

The design of the gap control loop was inspired by the work of Hicks and others (1984).

In this instrument, the microcontroller responsible for housekeeping measurements and configuration of the image sensor is not part of the gap control loop. Based on the FPI temperature, it calculates corrections to the gap setpoint values fed to the digital-to-analog converters. This way, gap variations caused by changes in temperature could be effectively attenuated.

6. Gap Instability

The dominant contributors to temperature induced variations of the FPI gap control are the following:

- *Gap measurement:*
  Area of measurement electrodes
  Deviation from electrode parallelism
  Reference capacitors
- *Setpoint voltage:*
  DAC gain and offset
  DAC buffer amplifier gain and offset
- *PSD and integrator:*
  Charge injection in switches
  Integrator offset

The temperature dependence of the piezo actuators and offset drift of the piezo amplifier are compensated by the PI-controller, and do not affect the gap. DC errors in the error amplifier do not affect the signal at the measurement frequency, and can be disregarded.

Thermal expansion of the fused silica substrates changes the area of the electrodes by a factor of approximately $2\,\alpha\,\Delta T$, where α is the coefficient of linear thermal expansion of the material. For fused silica, the coefficient of thermal expansion is given as 0.55 ppm/K (Roy et al., 1989), which translates to a relative area and capacitance change of 1.1 ppm/K. In addition to the direct area change, thermal expansion can cause deformation of the substrates that affects parallelism.

Drift of the reference capacitance, C_{ref}, directly modifies the bridge balance condition, Eqn. (2). The control loop compensates for this by changing the gap to regain balance. The reference capacitors used have a temperature coefficient specified to ±30 ppm/°C. Measurements on a number of capacitors showed a parabola-shaped capacitance change as a function of temperature. At low temperatures, the temperature coefficient was negative, increasing through zero at room temperature to positive values at higher temperatures. The measurement was carried out at a temperature range of 5 to 70°C. The highest temperature coefficient, 17 ppm/°C, was measured at 70°C (Näsilä, 2013).

The voltage feeding the lower arm of the half-bridge (Figure 3) is affected by the gain and offset variations of the DAC and the buffer amplifier. The AD5662 DAC and the AD8694 operation amplifier, both manufactured by Analog Devices, were used in the Aalto-1 Spectral Imager.

The transfer function of the DAC (output voltage as a function of digital input number) can be approximated by a linear function fitted to measured behavior in the linear region of operation. The intercept and slope vary with temperature, and are displayed in the data sheet as offset error drift and gain error drift. Typical values for this converter are ±3 µV/°C and ±2.5 ppm/°C, respectively. For a full-scale output of 2.5 V, the latter gives ±6 µV/°C.

The buffer amplifier is a non-inverting operational amplifier configuration with a gain of two. The offset voltage drift is specified to 6 µV/°C. In this circuit, the bias current is negligible. The feedback resistors have a temperature coefficient (TC) specified to ±50 ppm/°C. The gain of the buffer amplifier is determined by the ratio of two resistances. The given range of the temperature coefficient means the maximum TC over the specified temperature range. Often, the temperature coefficient tracking, i.e., the difference between the temperature coefficients of resistors at the same temperature, is considerably lower. Without explicit tracking specifications or component selection based on TC measurements, the worst combination is assumed here, however.

The output of the buffer amplifier is fed to the modulation switches. The effect of the switches on the temperature drift is considered negligible.

The amplified 312 kHz error signal is rectified in a phase-sensitive detector based on a clamp-and-sample design (Figure 6). The main error source in the PSD is a charge injection from the CMOS switches. The motivation for selecting this design was simple circuitry and the low number of components.

The rectified, demodulated error signal represents the input to the error integrator of the PI-controller—again, realized with an operational amplifier. This PI-controller determines the dynamics of the gap control loop. The resulting error introduced through charge injection in the PSD switches and input offset voltage of the operational amplifier was estimated by measuring the rate of change of the integrator output with a bridge error signal of zero. To keep the integrator output constant, the PSD errors must be compensated by an error signal of 18 mV at the PSD input. Taking the error amplifier gain of ten into account, the error compensation requirement at the measurement half-bridge is 1.8 mV. The temperature dependency of the required error signal was measured on a representative gap controller to 41 µV/°C at the PSD input in the temperature range 25 to 60°C. This corresponds to a gap drift of 0.017 nm/°C.

As such, the imbalance signal required to counteract the PSD offset invalidates the design idea of a null-detector; now, too, the gain of the error amplifiers affects the resulting gap. In this case, however, the effect is negligible compared to the other error sources.

The contribution to the gap drift of the error sources are summarized in Table 2. All contributions are given as positive numbers; the sum is thus a worst-case estimate.

The lack of information on the tracking of the resistances of the DAC buffer amplifiers causes the

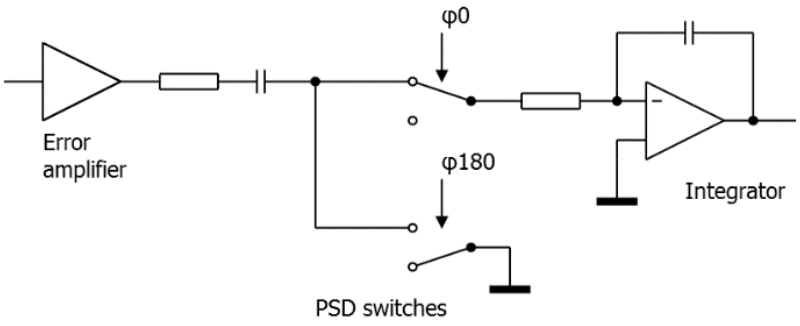

Figure 6. Clamp-and-sample-based PSD and integrator.

Table 2. Sources of Temperature Drift and Estimated Contributions

Source of error	Gap drift (nm/°C)
Electrode area	0.004
Reference capacitance	0.100
Offset of setpoint DAC	0.014
Gain of setpoint DAC	0.010
Offset of DAC buffer	0.028
Gain of DAC buffer	0.470
Charge injection of PSD switches and offset of integrator	0.017
Sum	0.644

highest drift value, as the worst combination of temperature coefficients was used. Measurements on a representative gap controller suggest that the contribution of the gain of the DAC buffer in Table 2 may be exaggerated.

The gap measurement is not influenced by humidity or air pressure, as the imager operates in vacuum conditions.

7. Gap Stability Measurements

During thermal vacuum testing of the Aalto-1 Spectral Imager, the gap was measured as a function of temperature (Figure 7). At temperatures below 20°C, the temperature coefficient of the gap was −2.4 nm/°C, increasing to −0.5 nm/°C above 30°C. The former value cannot be explained by drift induced by the electronics; de-formation of the substrates is a probable cause (Näsilä, 2013).

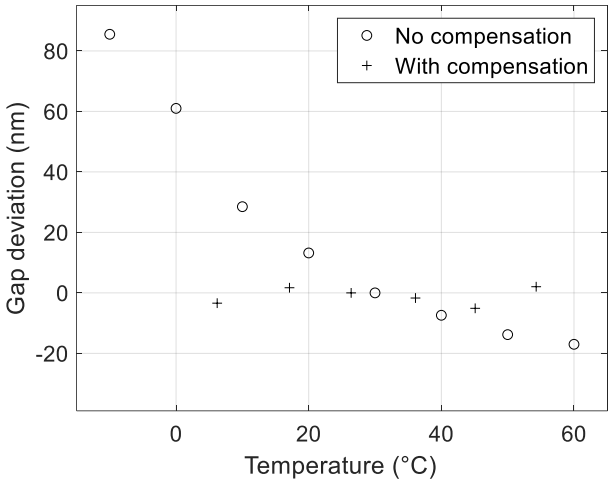

Figure 7. Variation of the gap from nominal at 30 °C, with and without temperature compensation (Näsilä, 2013).

It was found that the gap deviation was repeatable and could be predicted from the measured FPI temperature. A compensation function was written for the instrument microcontroller that calculates a correction for the setpoints based on the temperature. Using this temperature compensation function, the gap stability was improved by more than a factor of ten, clearly within the requirement 0.3 nm/°C (Figure 7).

Even if the mean gap deviation could be compensated for, the mirror deformation was still present, degrading the performance of the FPI at temperatures below 0°C. Figure 8 shows the standard deviation of the gap calculated over the 15 mm aperture at different temperatures.

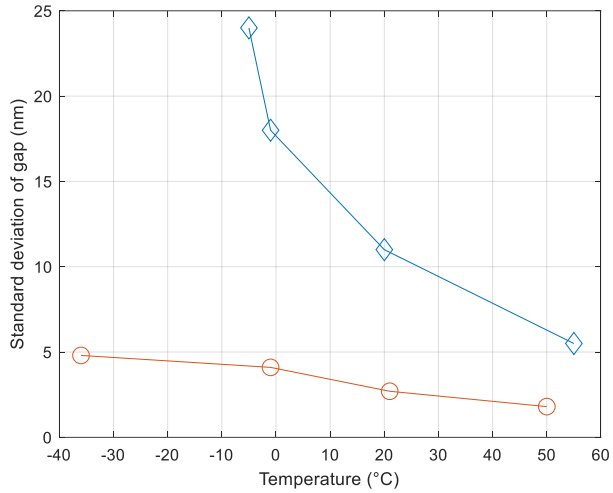

Figure 8. Standard deviation of the gap for Aalto-1 (diamonds) and Vision (circles).

In a more recent project, Picasso Vision, the manufacturing process of the FPIs was modified. This resulted in significant improvement in both the standard deviation of the gap and its temperature dependency.

8. Conclusions

Thermal testing of the Fabry-Perot interferometer used in the Aalto-1 Spectral Imager showed temperature-induced drift of the mirror gap of −2.4 nm/°C, exceeding the requirement. An error analysis of the gap control electronics showed the potential causes, but the total estimated error, 0.6 nm/°C, did not reach the measured values. The control scheme can only attempt to stabilize the capacitances, not the FPI gap. As the capacitive measurement of the FPI gap is made outside the optically active area, any deformation of the substrates cannot be compensated by the control loop.

The total gap drift was improved by letting the instrument microcontroller change the nominal control-

ler set-points with values calculated from the FPI temperature. Using this temperature compensation function, the stability of the FPI fulfilled the requirement.

Acknowledgements

Aalto University provided the possibility to include the Spectral Imager as one of the payloads of its nanosatellite Aalto-1. The Aalto-1 Spectral Imager was made by VTT Technical Research Centre of Finland under ESTEC Contract No. 4000106267/12/NL/CP.

The authors wish to acknowledge the work of Mr. Osmo Viljamaa for assembling the FPI control electronics used in the Aalto-1 Spectral Imager.

References

Hicks, T. R., Reay, N. K., and Atherton, P. D. (1984): The Application of Capacitance Micrometry to the Control of Fabry-Perot Etalons. *J. Phys. E: Sci. Instrum.*, Vol. 17, pp. 49–55.

Kestilä, A. et al. (2013): Aalto-1 Nanosatellite – Technical Description and Mission Objectives. *Geosci. Instrum. Method. Data Syst.*, Vol. 2, pp.121–130.

Kohouta, T. et al. (2018): Feasibility of Asteroid Exploration Using CubeSats – ASPECT Case Study. *Advances in Space Research*, Vol. 62 (8), pp. 2239–2244.

Mannila, R. et al. (2013): Spectral Imager Based on Fabry-Perot Interferometer for Aalto-1 Nanosatellite, in *Proc. SPIE 8870, Imaging Spectrometry XVIII*, San Diego, CA, Sept. 23.

Näsilä, A. (2013): Validation of Aalto-1 Spectral Imager Technology to Space Environment, Master's thesis. Aalto University. Available at: https://aaltodoc.aalto.fi/bitstream/handle/123456789/10451/master_N%C3%A4sil%C3%A4_Antti_2013.pdf (accessed Jan. 5, 2019).

Näsilä, A. (2016): PICASSO VISION Instrument Design, Engineering Model Test Results, and Flight Model Development Status, in *Proc. SPIE 10001, Remote Sensing of Clouds and the Atmosphere XXI*, Edinburgh, UK, Oct. 1916.

Reaktor Space Lab (2019): Seeing the Invisible – Hello World's Hyperspectral Imaging Capabilities Explained" (February 17). Available at: https://reaktorspace.com/2019/02/17/seeing-the-invisible-hello-worlds-hyperspectral-imaging-capabilities-explained/ (accessed Jun. 9, 2019).

Rees, D. et al. (1981): A Stable, Rugged, Capacitance-Stabilised Piezoelectric Scanned Fabry-Perot Etalon. *J. Phys. E: Sci. Instrum.*, Vol. 14, pp. 1320–1325.

Remy, B. et al. (2019): The ALTIUS System Performance Simulator, in *Workshop on Simulation and EGSE for Space Programmes (SESP)*, Mar. 26–28, 2019, ESA-ESTEC, Noordwijk, the Netherlands. Available at: https://www.researchgate.net/publication/331650575_The_ALTIUS_System_Performance_Simulator_End-to-end_Performance_Simulation_of_the_ALTIUS_Limb_Sounder_Spectrally_Tuneable_Optical_Imaging_System/download (accessed Jun. 6, 2019).

Roy, R., Agraval, D. K., and McKinstry, H. A. (1989): Very Low Thermal Expansion Coefficient Materials. *Annu. Rev. Matr. Sci.*, Vol. 19, pp. 59–81.

Saari, H. et al. (2015): Visible Spectral Imager for Occultation and Nightglow (VISION) for the PICASSO Mission, in *Proc. SPIE 9639, Sensors, Systems, and Next-Generation Satellites XIX*, Toulouse, France, Oct. 20.